

Multi-scale pore morphology in directed vapor deposited yttria-stabilized zirconia coatings

D.D. Hass^{a,*}, H. Zhao^a, T. Dobbins^b, A.J. Allen^c, A.J. Slifka^d, H.N.G. Wadley^a

^a Department of Materials Science and Engineering, School of Engineering and Applied Science, University of Virginia, Charlottesville, VA 22903, USA

^b Department of Physics, Louisiana Tech University, Ruston, LA 71270, USA

^c Ceramics Division, National Institute of Standards and Technology, Gaithersburg, MD 20899, USA

^d Materials Reliability Division, National Institute of Standards and Technology, Boulder, CO 80305, USA

ARTICLE INFO

Article history:

Received 28 December 2009

Received in revised form 7 June 2010

Accepted 12 June 2010

Keywords:

Electron beam evaporation

Scanning electron microscopy (SEM)

Zirconium oxide

Yttrium oxide

Thermal conductivity

Ultra-small-angle X-ray scattering

Directed vapor deposition

ABSTRACT

A high pressure, electron-beam directed-vapor deposition process has been used to deposit partially stabilized zirconia containing 7% mass yttria at deposition pressures of 7.5–23 Pa. Anisotropic, ultra-small-angle X-ray scattering (USAXS) was then used to determine the surface area, shape and orientation of pores within the coatings. The total surface area of the ellipsoidal shaped pores was found to increase with deposition pressure. However, the through-thickness thermal conductivity measurements reveal the existence of a minimum thermal conductivity in coatings deposited at an intermediate pressure. Observations of the anisotropic X-ray scattering intensity at this intermediate pressure indicated greater proportions of both feather-like (oblate) pores with their major dimension at about 60° to the plane of the coating and fine columnar (prolate) pores oriented perpendicular to the coating plane. Since these oblate pore orientations are most efficient at impeding conductive thermal transport through the coating, it is believed that the change in preferred pore orientations with pressure is responsible for the higher thermal resistance of coatings grown in the intermediate pressure regime.

© 2010 Elsevier B.V. All rights reserved.

1. Introduction

Thermal barrier coatings (TBC's) are widely used for protecting hot structures in gas turbine engines [1–4]. These coatings use a thermally insulating ceramic layer to impede heat flow and a metallic undercoating (a bond coat) to improve ceramic layer adhesion by impeding oxidation and hot corrosion. When these coating systems are applied to internally cooled components, the temperature drop across the ceramic layer depends on the coating thickness and its through-thickness thermal conductivity. Coatings of 150 μm thickness and thermal conductivities in the 1.5–2 $\text{W m}^{-1} \text{K}^{-1}$ range have been shown to provide significant metal surface temperature reductions [2,3]. There is significant interest in developing thermal barrier coatings with lower thermal conductivities provided this does not adversely affect other coating attributes such as spallation and erosion resistance [5].

Yttria-stabilized zirconia (YSZ) is the most widely used ceramic for TBC applications [2]. Thermal transport in this material occurs by a combination of conduction [6,7] and radiative transport (the material is partially transparent at optical and near infrared wavelengths) [8,9]. The radiative transport process is important at high

temperatures. At lower temperatures, conductive transport dominates, and the thermal resistance can be improved by enhancing phonon scattering [8]. At the atomic scale, this can be accomplished by adding atoms of different atomic mass to the crystal lattice and incorporating imperfections such as vacancies [6,7,8,10,11]. Fully dense zirconia partially stabilized with about 7% mass yttria (7YSZ) has an ambient temperature thermal conductivity of $\approx 3 \text{ W m}^{-1} \text{K}^{-1}$ as a result of the yttrium solute addition and the formation of O^{2-} vacancies that are required to maintain electrical neutrality within the ionically-bonded lattice.

Further reductions in thermal conductivity can be achieved by incorporating porosity in the coating. Recent experimental and modeling studies have shown the thermal conductivity of 7YSZ to be a strong function of the pore volume fraction, the pore shape, the pore size and the pore distribution [12]. In porous coatings, conductive heat transfer across a single pore occurs by conduction through and around the pores. Obviously, increasing the pore volume fraction for a given pore size and shape will decrease the thermal conductivity. However, the pore shape is also important. Elongated (prolate) pores oriented so that their long axes are perpendicular to the heat flux have been shown to be more effective at impeding heat transfer than a sphere of equivalent volume [13]. Similarly, flattened (oblate) pores are more effective if aligned so that their short axis is parallel to the heat flux direction.

* Corresponding author. Fax: +1 434 977 1462.

E-mail address: derekh@directedvapor.com (D.D. Hass).

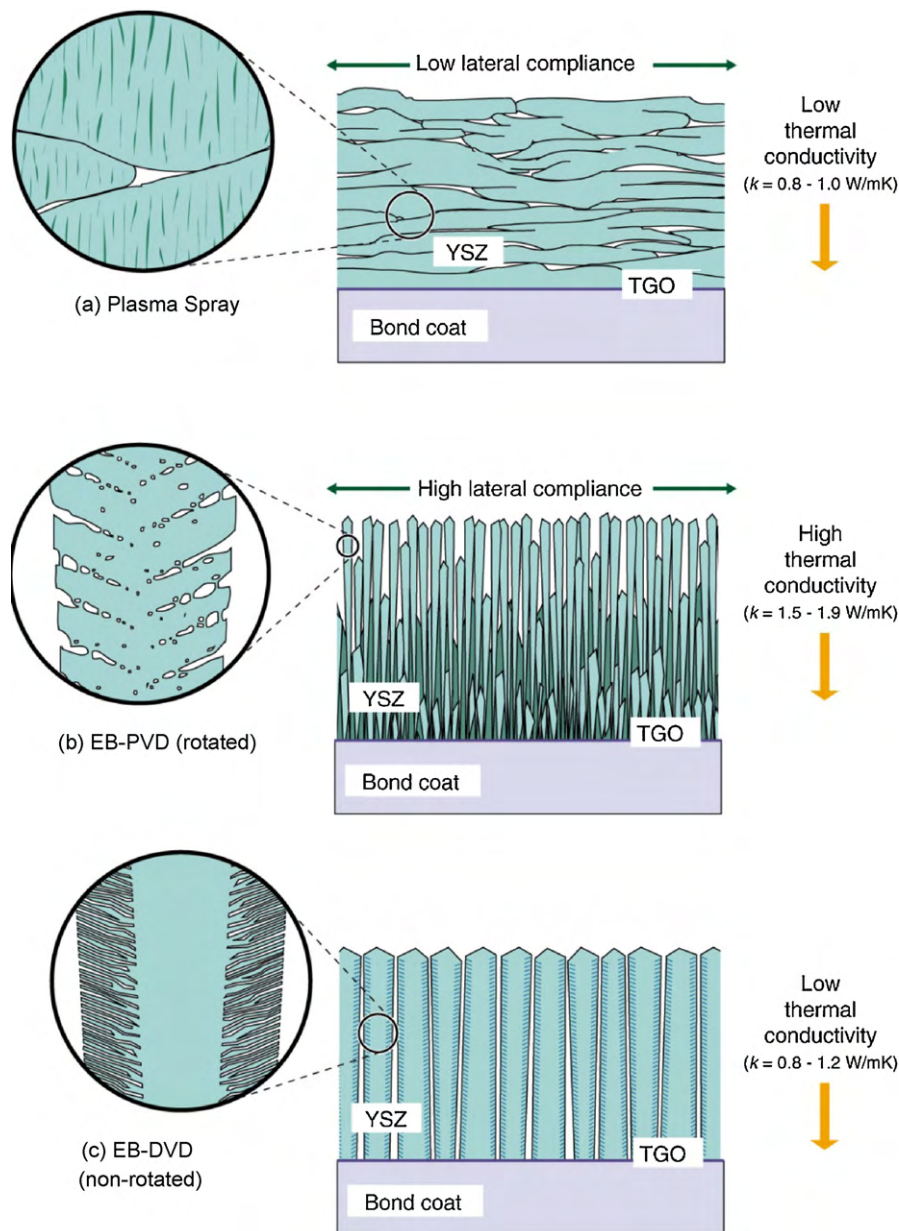


Fig. 1. Schematic illustration of the pore morphology of YSZ coatings made by (a) air plasma spray (APS) (b) electron beam – physical vapor deposition (EB-PVD) and (c) by the EB-DVD process. Their thermal conductivities are influenced by the process used to deposit them.

Porous 7YSZ coatings are usually deposited by either air plasma spray (APS) or electron beam – physical vapor deposition (EB-PVD) [1,2]. However, the coatings made by these two approaches have quite different pore volume fractions and shapes, see Fig. 1. The APS process creates coatings by the repeated impingement of semi-molten droplets onto the substrate. This results in the formation of oblate pores that are flattened in the plane of the substrate. These pores are highly effective at impeding the flow of the heat normal to the coating surface. As a result, the through-thickness thermal conductivity of these coatings is in the $0.8\text{--}1.0 \text{ W m}^{-1} \text{ K}^{-1}$ range (when measured at 25°C) and is well below that of dense 7YSZ [14–16]. In EB-PVD, components are rotated in a vapor plume and so condensation of the vapor molecules usually occurs under oblique molecular incidence conditions. This leads to local self-shadowing by small regions of faster growing regions on the coating

surface and the development of porous columnar coating structures. The columns in these coatings are highly textured and the primary inter-columnar pores are elongated with their long axes orientated perpendicular to the plane of the coating. This alignment increases the coating's in-plane elastic compliance resulting in a microstructure that is more robust under thermal cycling than those produced with APS. Finer scale pores ($<1 \mu\text{m}$ in diameter) are also present within the columns. These include nanoscale spherical pores and groups of pores between the columns that are inclined at about 30° to 40° to the column axis. These feathery pore structures impede the transport of heat, and the through-thickness thermal conductivity of EB-PVD coatings lies in the $1.5\text{--}1.9 \text{ W m}^{-1} \text{ K}^{-1}$ range at 25°C [17]. The study reported here is motivated by an interest in high pressure, vapor deposited coating microstructures that have thermal conductivities below those of EB-PVD coat-

ings while retaining the high in-plane compliance needed in high spallation lifetime applications where cyclic thermal loading is severe.

Recent experimental and atomistic modeling studies have shown that the pore morphologies in vapor deposited coatings are affected by many “process related” variables including the vapor atoms’ kinetic energy [18,19] and incidence angle [20,21], the substrate temperature [22,23], the deposition rate [21,23], the background pressure [21,24,25], the vapor plume composition [26] and the substrate’s initial roughness [27]. Experimental studies indicate that the porous, columnar morphologies are associated with low kinetic energy, oblique vapor incidence angles, low substrate temperatures, high deposition rates, rough substrates and high chamber pressures [17,19,21,27,28]. Atomistic models of coating growth support these observations [29] and have begun to quantify the linkages between pore formation, surface roughness and flux shadowing under conditions of restricted surface atom mobility [30].

A gas jet assisted directed-vapor deposition (DVD) approach has recently been proposed as a means to access coating conditions that promote pore formation, and this technique is being explored for the synthesis of thermal barrier coatings [31]. In this approach, a trans-sonic helium gas jet is used to entrain and transport 7YSZ vapor created by the impingement of an electron beam upon a source material. The deposition of this entrained vapor occurs at much higher pressures (10–100 Pa) than conventional EB-PVD processes. Binary collision theory indicates that the mean-free-path of zirconia molecules in these helium jets decreases from ≈ 10 m to ≈ 1 mm as the background pressure is increased from 10^{-3} Pa to 10 Pa [32]. This scattering of the vapor molecules during transport towards a substrate broadens the angular divergence of the vapor flux during deposition. This increases the probability that a molecule impacts a surface asperity and promotes void formation. As the gas jet density (pressure) increases, the probability of nucleating vapor phase clusters also rises. Columnar structures can still be created during cluster deposition but a significant fraction of the porosity is in the form of uniformly distributed nanoscale pores. The DVD technique therefore allows the synthesis of columnar microstructures whose pore volume fraction and morphology can be manipulated over wide ranges by modification of the gas jet conditions [33].

Characterization of the pore structure within a thermal barrier coating is complicated by the wide variations in pore morphology (pore shape), pore orientation, inter-pore separation and pore size distribution. Multi-scale measurements of the structure are therefore required. These measurements can then be analyzed to provide estimates of quantities defined by appropriate models of the coating structure. Scanning electron microscopy provides sufficient information to construct a prototypical model structure. However, it is difficult to quantify the parameters that define the pore structure from these surface observations. X-ray scattering measurements using a transmission geometry provide an alternative approach. X-rays are scattered when they traverse samples containing regions of reduced electron density (pores) and so measurements of the scattering pattern around the directly transmitted beam provide information about the Fourier transform of the scattering sources. The emergence of high flux, well collimated monochromatic X-ray sources at various synchrotron sources provides a powerful means of probing significant sample volumes and obtaining statistically significant estimates of the pore populations [34].

Here, an electron-beam DVD method has been used to deposit 7YSZ coatings grown using various jet flow conditions. Scanning electron microscopy and ultra-small-angle X-ray scattering techniques (USAXS) have then been used to investigate the morphology of the pores over the scale range from 50 nm (down to 10 nm in

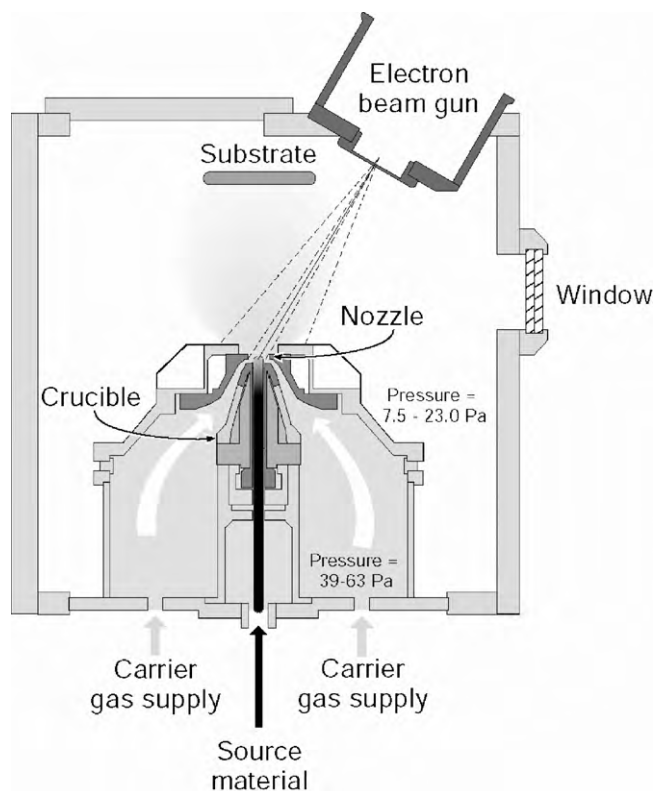


Fig. 2. A schematic diagram of the directed vapor deposition process. A high voltage (70 kV) electron beam is to evaporate a 7YSZ source material which is then entrained in a helium gas jet and deposited upon a heated substrate. The gas jet is formed by the supersonic expansion of a carrier gas through an annular nozzle that surrounds the vapor emitting tip of the source material.

opening dimension) to 1 μm in diameter. These techniques enable information to be obtained about the pore surface area, pore shape and the pore orientation distribution as a function of pore size. The density and thermal conductivity of the coatings have also been measured and linked to the pore morphology parameters deduced from the USAXS analysis. Through such analysis, the significant effect of the jet flow conditions on the coating pore population and thermal conductivity can be demonstrated.

2. Experimental methods

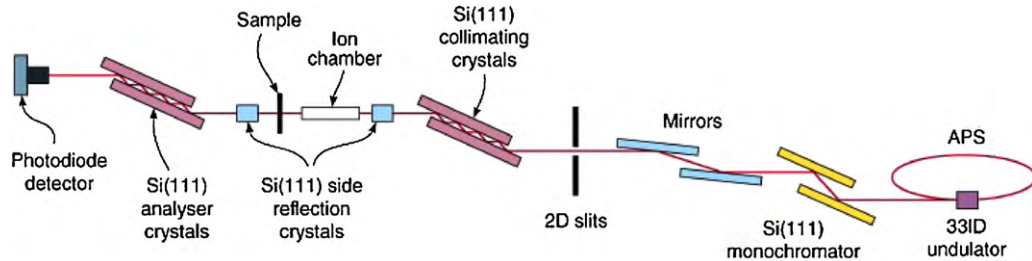
2.1. 7YSZ deposition

An electron beam – DVD processing technique, Fig. 2, has been used to make coatings from a 7YSZ source [31,35,36]. Three combinations of process conditions were used to create samples with densities between 3.4 g cm^{-3} and 4.4 g cm^{-3} and different pore orientations. Material was vaporized using a high voltage (70 kV), medium power (10 kW) axial e-beam gun. By incorporating differential pumping of the gun column and using a small (3 mm diameter) electron beam aperture gun, an intense electron beam could be introduced into a relative pressure chamber and used for source material evaporation. A gas jet was created around the evaporation source by the expansion of helium through a 30 mm outer diameter annular nozzle surrounding the evaporation source. Supersonic expansion was achieved by maintaining an upstream to downstream (chamber) pressure ratio in excess of two. For the samples studied here, the flow rate of the helium carrier gas was held constant at 5.0 standard liters per minute (slm) and the chamber pumping rate was varied resulting in jet flow conditions where the upstream to downstream pressure ratio varied from 1.7 to 7.9

Table 1

Process conditions used for 7YSZ coating deposition at 1050 °C.

Sample	Chamber pressure (Pa)	Upstream pressure (Pa)	Gas jet speed (m s ⁻¹)	Deposition rate ((m min ⁻¹))	Coating thickness (μm) ^a
A	7.5	59	1999	15	746
B	13.0	63	1656	12	279
C	23.0	39	856	20	223

^a As measured at the center point of the substrate.**Fig. 3.** Diagram of the experimental set-up used to perform USAXS measurements [37,38].

and chamber pressure changed from 7.5 Pa to 23.0 Pa (Table 1). The vapor from the source was entrained in these gas jets and transported to 25.4 mm diameter, platinum aluminate coated, Rene N5 substrates (GE Aircraft, Cincinnati, Ohio)¹.

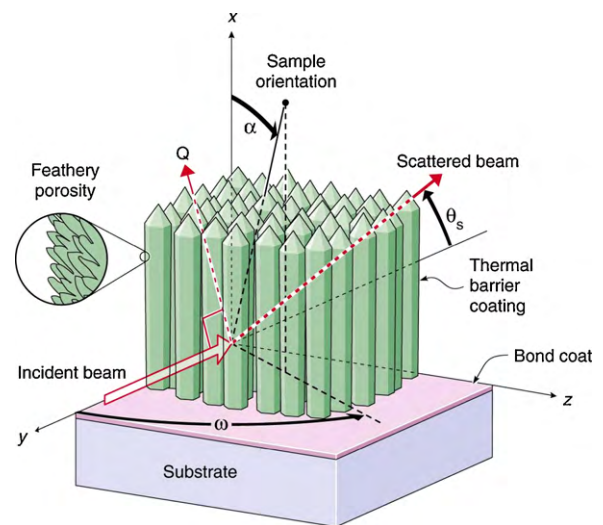
Vapor deposition onto stationary (non-rotated) substrates was performed using a source to substrate distance of 15.0 cm. To compensate for oxygen lost from the source during evaporation and vapor transport, a helium jet containing 3.0% by volume oxygen was used to create the gas jet. The jet speed at the nozzle opening depends only upon the up and downstream pressures and ratio of specific heats for the gas [32] and is provided in Table 1. A resistive heater placed behind the substrate was used to heat the substrates to 1050 °C during deposition. To enable analysis by the USAXS approach, deposition was continued until a flat sample with a coating thickness of at least 200 μm was achieved. The deposition rate depended upon the jet density and varied from 12.0 μm min⁻¹ to 20.0 μm min⁻¹.

2.2. Ultra-small-angle X-ray scattering

Ultra-small-angle X-ray scattering (USAXS) measurements were conducted using the USAXS instrument built by NIST in partnership with the Advanced Photon Source [37], and presently located at XOR sector 32-ID of the Advanced Photon Source, Argonne National Laboratory, Argonne, IL. The basic set-up is schematically illustrated in Fig. 3. Ref. [38] provides a detailed description of the USAXS instrument and the measurement method. This instrument utilizes a Bonse-Hart double-crystal X-ray optical system [37–39] to extend the range of low angle scattering vectors that can be experimentally obtained using a small angle scattering approach. In its modified form (see below) this instrument enables anisotropic structural information (including that of porosity) to be measured along the direction of the scattering vector, \mathbf{Q} (where $|\mathbf{Q}| = (4\pi/\lambda)(\sin \theta)$ and θ is half of the scattering angle, θ_s), over a large range of length scales (≈ 10 nm to ≈ 2 μm). From each coating listed in Table 1, thin sections (< 200 μm thick) were cut orthogonal to the substrate plane. Each section was mounted in the USAXS instrument perpendicular to the incident X-ray beam such that the $100 \mu\text{m} \times 100 \mu\text{m}$ X-ray beam was centered on the

section (i.e. centered within the coating thickness indicated in Table 1). The scattering geometry used is defined in Fig. 4. Note that the direction of \mathbf{Q} bisects the scattering angle, which is always small. Thus, the \mathbf{Q} direction lies approximately in the sample plane perpendicular to the incident beam, and in the same azimuthal direction as the scattered beam (vertical in the USAXS instrument). The different azimuthal angles, α , are selected by rotating the sample orientation around the incident beam direction prior to the USAXS scan with ω set to 90°.

USAXS measurements exploit crystal diffraction optics to provide a finely collimated and highly monochromatic X-ray beam. Using Si (1 1 1) monochromator crystals, the X-ray energy selected was 16.9 keV, just below the anomalous absorption edge for yttrium. Using a transmission geometry, the small-angle scattering intensity was measured using a photodiode detector positioned behind the Si (1 1 1) crystal analyzer stage as this crystal was rocked through and away from the Bragg diffraction angle (zero \mathbf{Q}). Samples were centered on the rotational axis of an azimuthal rotation stage, which was centered on the X-ray beam. The intrinsic slit-smeared geometry found in standard USAXS measurements was removed experimentally using orthogonal diffracting crystals.

**Fig. 4.** Geometric relations between the anisotropic coating's crystal orientation and the incident and scattered radiation beams. With $\omega = 90^\circ$, the sample orientation around the incident beam direction could be rotated in the x - z plane to give values of α from 0° to 360° .

¹ Certain commercial materials and equipment are identified in this paper to specify adequately the experimental procedure. In no case does such identification imply recommendation by NIST nor does it imply that the material or equipment identified is necessarily the best available for this purpose.

Two types of measurement data were collected. For the first, the scattering intensity was measured as a function of Q for several orientations of the azimuthal angle, α . For the second, the scattering intensity at a particular Q was measured as a function of α by rotating the sample in the beam. In both cases the data were reduced and analyzed using the USAXS instrument *Irena* software package [40]. The software package computes absolute-calibrated USAXS intensity, $I(Q)$ versus Q data with an estimate of the standard deviation uncertainties, based on the scattering intensities measured. Anisotropy in the scattering at different Q values reveals information about the anisotropic coating microstructure in a given scale range. At small Q values, the scattering intensity (which is proportional to the squared difference in electron density between the two materials), the pore volume fraction and the pore volume determine the scattering intensity. Thus, larger feature (pore) sizes dominate the scattering intensity in this region. At high Q , fine nanoscale pores dominate the scattering intensity, and the total specific surface area of the pores can be derived from an anisotropic orientational average of the terminal Q^{-4} slope of the intensity as a function of Q (Porod scattering) [41] after the flat background scattering has been subtracted.

2.3. Thermal conductivity measurements

The thermal conductivity, κ , of the 7YSZ coatings was measured using a direct steady state approach [42–44]. The technique employed an infrared thermal microscope and infrared laser heating to determine the thermal conductivity of a sample using a variation of ASTM 1225-87 (commonly known as the cut-bar approach) [45]. In the cut-bar approach, a specimen of unknown thermal conductivity is sandwiched between two materials with known thermal conductivities. By applying heat in the direction parallel to the material interfaces and measuring the temperature along the length of the three materials, the heat flow rate may be inferred and used to determine the thermal conductivity of an unknown specimen using:

$$q = -\kappa A(\Delta T/\Delta X) \quad (1)$$

where q is the heat rate applied (W), κ is the thermal conductivity ($\text{W m}^{-1} \text{K}^{-1}$), A is the cross-sectional area that the heat flows through (m^2), and $\Delta T/\Delta X$ is the temperature gradient (K m^{-1}) over the distance that heat flow is measured. In the approach used for this work, the temperature difference across a fixed, known distance of the substrate was measured using an infrared (IR) microscope. This, in conjunction with the known thermal conductivity of the substrate material and Eq. (1) were used to calculate q . The thermal conductivity of the coating could then be determined by measuring $\Delta T/\Delta X$ across the thickness of the coating. The validity of this testing methodology, including a determination of the experimental uncertainties, has been confirmed using a guarded hot plate approach (ASTM C177-85) [46]. The testing methodology used for the present study was ideal as it directly measured the thermal conductivity of a ceramic coating, was relatively fast (guarded hot plate approaches often required greater than 130 h to perform [47]) and could be applied to small samples (3 mm \times 3 mm) making a study of the effect of pore morphology on the thermal conductivity of TBC layers feasible. For further details on this measurement approach the reader is referred to Ref. [48].

2.4. Density measurement

The coating density was determined directly from coating mass and thickness measurements. Measurements were performed on 9.0 mm² area samples cut from the central region of the 25.4 mm diameter substrates. For each sample, the sides were polished to better than 800 grit to yield a smooth cross-section from which

the sample dimensions could be determined using a calibrated SEM. Thickness measurements were made at 200 μm intervals around the periphery of the samples, allowing both an average coating thickness and its statistical standard deviation uncertainty to be determined. The samples were then cleaned in methanol and dried in an oven at 150 °C for 4 h to remove residual moisture in the coating. An initial mass of the sample was measured using a precision microbalance. The coating was then removed by etching in concentrated hydrofluoric acid for 30 min. The final mass of the substrate was measured and the density determined.

3. Results

3.1. Coating microstructures

All of the 7YSZ coatings had a columnar microstructure. Fig. 5 shows polished cross-sections of the growth columns for samples grown using the three chamber pressures (7.5 Pa, 13 Pa and 23.0 Pa). The sides of the primary growth columns remained approximately parallel during growth and so their diameters did not generally vary with thickness as schematically indicated in Fig. 4. The morphology of the sides and top of the growth columns are shown in Fig. 6 for the three coatings. These columnar structures are unlike those formed in EB-PVD which contain growth columns with tapered cross-sections as a consequence of a highly competitive column growth mode [7]. Here, elongated, inter-columnar pores up to $\approx 2 \mu\text{m}$ in width were present at the primary column boundaries and extended from the substrate to the coating's outer surface. The primary columns had a fractal structure with each column subdivided into small (sub) columns each separated by narrower intra-columnar pores.

The sides of the primary growth columns contain inclined pores that deeply penetrate into the column interiors at an angle of approximately 30° to the growth direction (60° to the substrate plane). SEM images of the polished coatings, Fig. 5, reveals that at the lowest pressure (7.5 Pa) the column surface pores were very small (extending below the resolution of the microscope) and as a result the columns appeared relatively smooth. As the chamber pressure was increased the intra-columnar pore structures increased in diameter resulting in a feathery appearance with the size of the “feathers” increasing with chamber pressure. However, the pore size and inter-pore spacing within the feathers was very difficult to resolve by the SEM technique. The column tips were also altered by the chamber pressure consistent with other observations of changes to the column texture with deposition conditions [31]. X-ray diffraction measurements, shown in Fig. 7, indicated a pronounced [1 1 1] texture in the sample grown at intermediate pressure whereas the other samples had a more random growth column texture.

3.2. USAXS measurements

By carrying out an orientational averaging of the scattering in the (high Q) Porod regime the total surface area per unit volume of pores (in the 50 nm to 2 μm diameter range) can be determined for each coating sample [41]. This measurement includes the scattering from all pore morphologies, and these Porod surface area data are given in Table 2. The pore surface area was found to increase with chamber pressure from 16.5 m² cm⁻³ to 72.1 m² cm⁻³ as the chamber pressure increased. For the highest pressure case (23 Pa) the sample was measured in two orthogonal orientations (Y and Z), see Fig. 4. It was found that this coating was not completely axially symmetric about the axis normal to the substrate because the growth columns were slightly inclined to the substrate normal. The

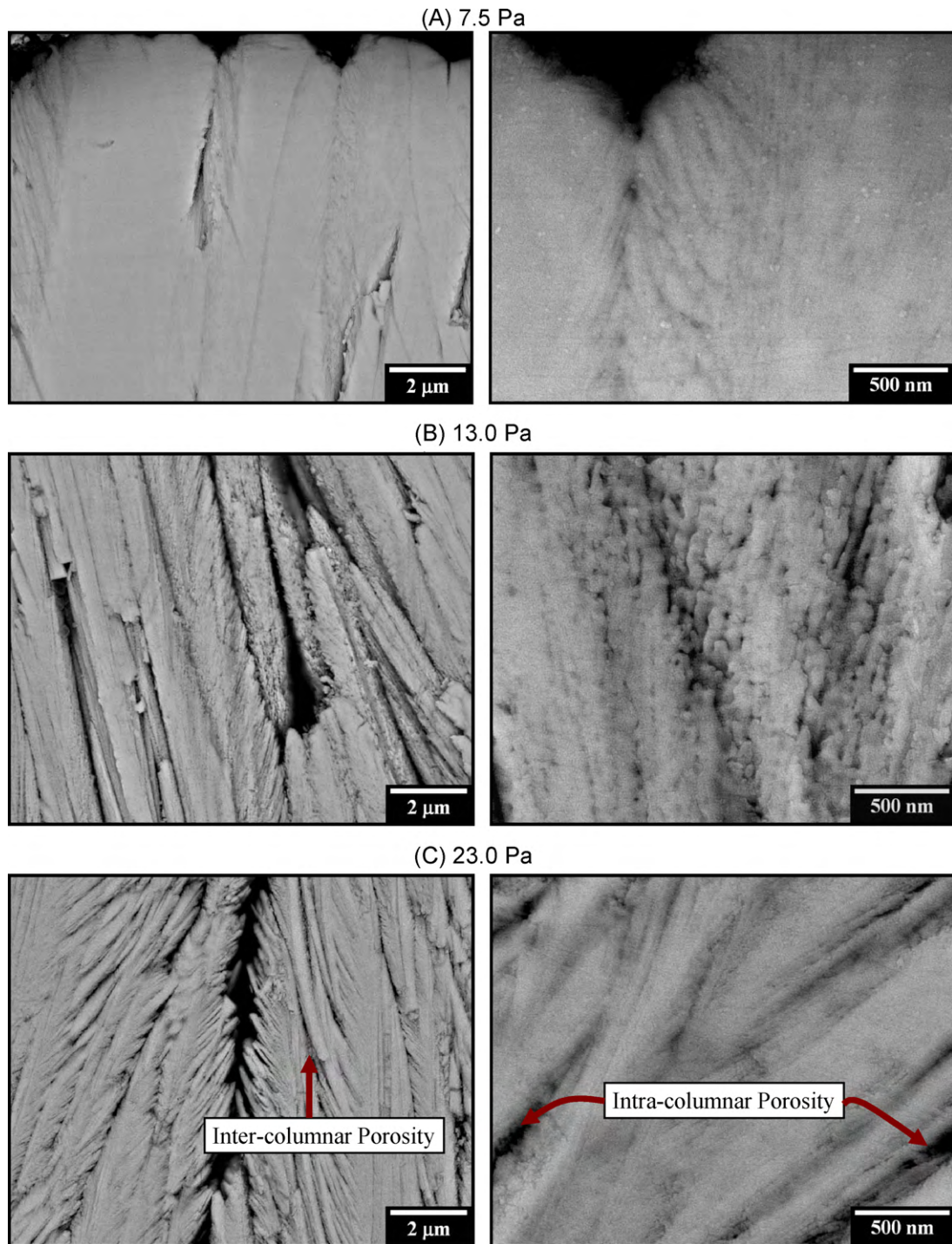


Fig. 5. Scanning electron micrographs of the cross-section of 7YSZ coatings deposited at chamber pressures of (a) 7.5 Pa, (b) 13.0 Pa and (c) 23.0 Pa.

Table 2

Summary of surface area measurements.

Sample	Chamber pressure (Pa)	Porod surface area (Z-direction) ($\text{m}^2 \text{cm}^{-3}$) ($\pm 5\%$)	Porod surface area (Y-direction) ($\text{m}^2 \text{cm}^{-3}$) ($\pm 5\%$)	Porod surface area (average) ($\text{m}^2 \text{cm}^{-3}$) ($\pm 5\%$)
A	7.5	16.6	–	16.6
B	13.0	33.7	–	33.7
C	23.0	57.8	86.4	72.1

Surface area uncertainties given are estimated standard deviations based on repeated measurements both here and in comparable anisotropic Porod scattering measurements [34].

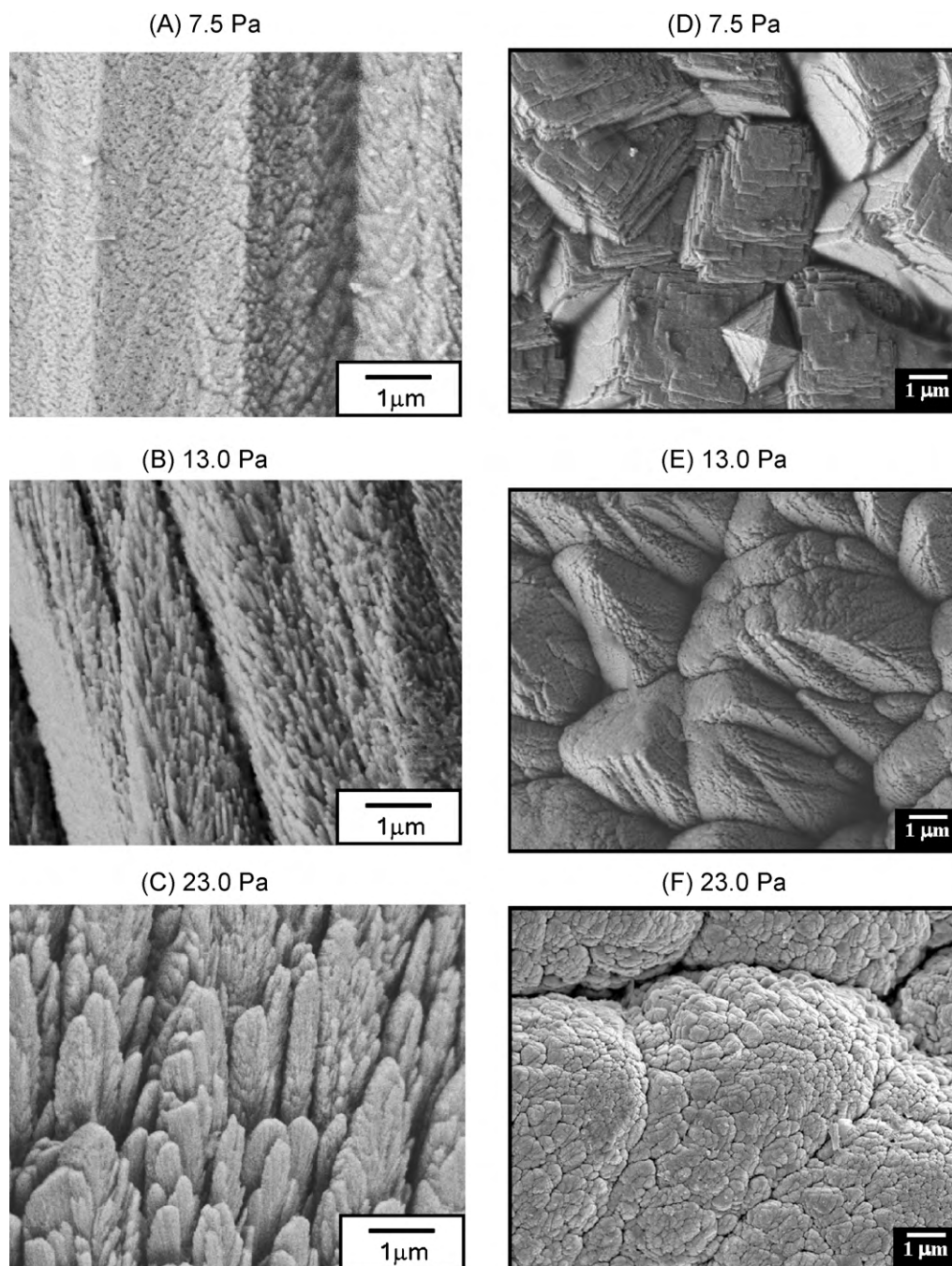


Fig. 6. Scanning electron micrographs of fractured cross-sections (a–c) and the top surfaces (d–f) of 7YSZ coatings deposited at chamber pressures of 7.5 Pa, 13.0 Pa and 23.0 Pa.

data in Table 2 for this condition are therefore given as an average of the two measurements.

Plots showing the change in the relative intensity of the X-ray scattering as a function of the magnitude of the scattering vector Q are given in Figs. 8–10. (Fig. 8 includes model fits discussed later.) The measured scattering intensity from a given pore size is inversely related to Q so that comparisons of the scattering intensity versus Q plots for each coating aligned at a given sample orientation of interest yields information about the volume fraction of pores of different size and shape in the coatings. Such plots were measured at three sample orientations: (i) with the Q direction parallel to the substrate surface, $\alpha \approx 90^\circ$, (case I, Fig. 8), (ii) with the Q direction aligned 60° from the substrate normal, $\alpha \approx 60^\circ$, i.e., 30° away from the plane of the substrate surface (case II, Fig. 9), and (iii)

with the Q direction perpendicular to the substrate surface, $\alpha = 0^\circ$ (case III, Fig. 10). The Q direction alignment parallel to the substrate surface provides scattering from structures within the plane of the substrate (in-plane structure). This is dominated by pores with their large dimensions in the plane perpendicular to the substrate, which in this case means the inter-columnar pores. With the Q direction aligned 30° to the substrate surface ($\alpha \approx 60^\circ$), the scattering is dominated by the contribution from the feathery pores. When the Q direction is aligned perpendicular to the substrate the scattering is dominated by structural variation through the coating thickness (out-of-plane structure), which may comprise globular pores or pores with their large dimensions in the substrate plane.

In case I, the shape of the scattering intensity curve was similar for both the low (7.5 Pa) and high (23.0 Pa) pressure conditions

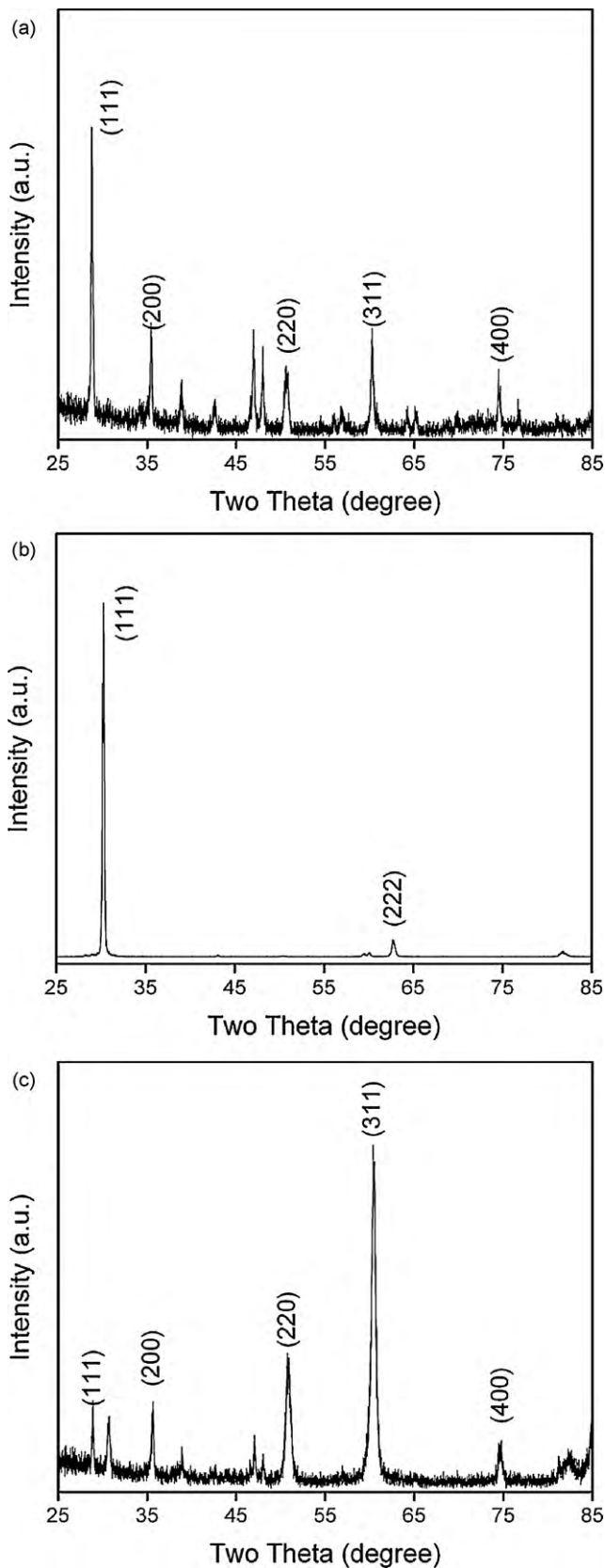


Fig. 7. X-ray diffraction patterns of the 7YSZ coatings deposited at chamber pressures of (a) 7.5 Pa, (b) 13.0 Pa and (c) 23.0 Pa. Patterns were obtained using Cu K α radiation (Q direction perpendicular to the substrate.).

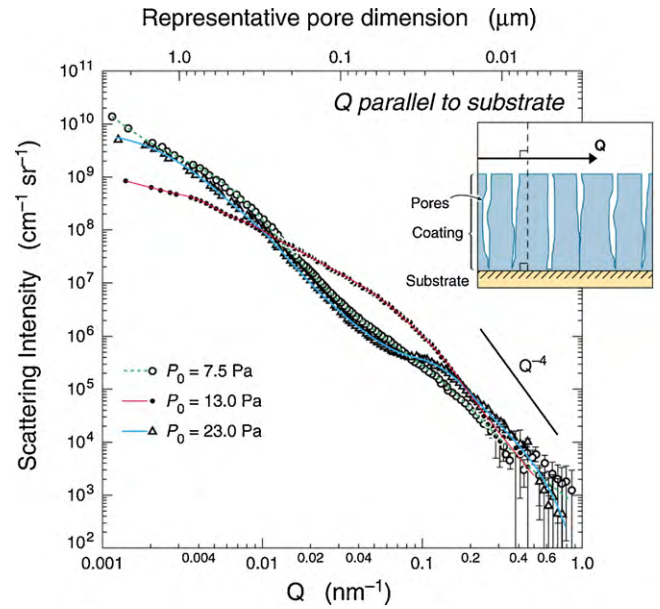


Fig. 8. Logarithmic plots of the absolute-calibrated scattering intensity versus the magnitude of the scattering vector, Q . Data collected with Q approximately parallel to the substrate is shown for each of the pressure conditions used to grow the coatings. In this and the following figures, experimental uncertainties are indicated by the scatter in the data, and are comparable to those shown in Figs. 9 and 10. The lines are MaxEnt fits to the data, discussed later in the text.

explored. Clear evidence was present for two scattering components, attributed to the primary inter-columnar pores and the finer intra-columnar (or sub-columnar) voids, respectively. Only small changes between these two conditions were observed with the scattering intensity for the 7.5 Pa case slightly stronger at low Q values ($<0.05 \text{ nm}^{-1}$), which corresponds to columnar pores with opening (small) dimensions $>100 \text{ nm}$ and large columnar dimen-

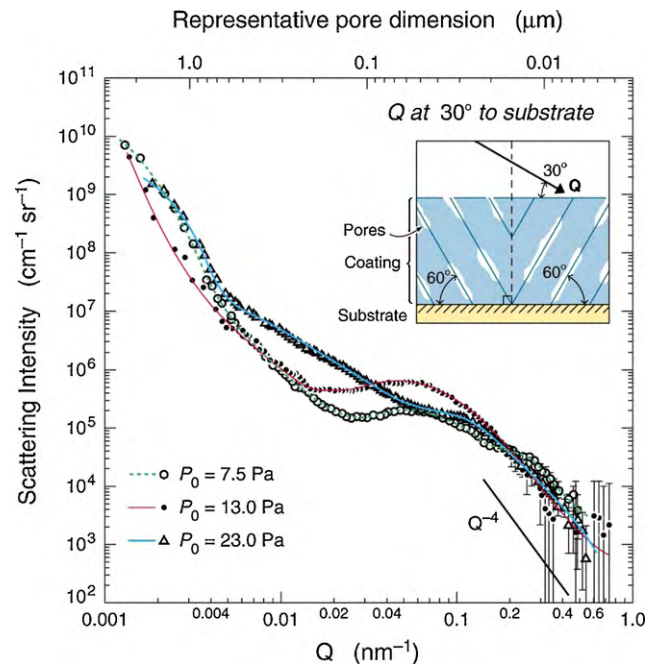


Fig. 9. Logarithmic plots of the absolute-calibrated scattering intensity versus the magnitude, Q , of the scattering vector for each of the pressure conditions used to grow the coatings with Q at an angle of approximately 30° to the substrate (60° from the substrate normal). The lines are guides to the eye, and a Q^{-4} power law is indicated at high Q to demonstrate how the surface areas were obtained.

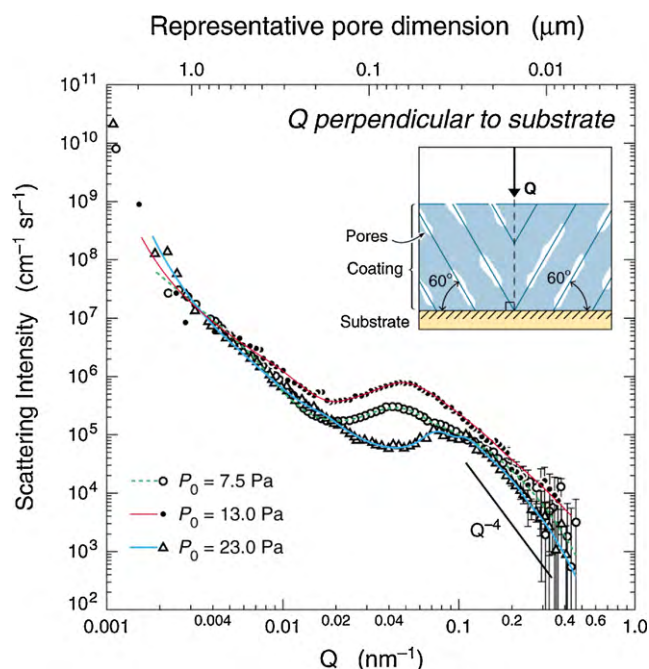


Fig. 10. Logarithmic plots of the absolute-calibrated scattering intensity versus the magnitude, Q , of the scattering vector for each of the pressure conditions used to grow the coatings with Q approximately perpendicular to the substrate. The lines are guides to the eye, and a Q^{-4} power law is indicated at high Q to demonstrate how the surface areas were obtained.

sions perhaps $1.0 \mu\text{m}$ or more in size. At high Q values, the situation was reversed, with the high pressure (23.0 Pa) condition giving stronger scattering (corresponding to more surface area or apparent porosity) from the fine intra-columnar pores with opening (small) dimensions of about 20 nm . Note that it is the stronger Porod scattering at high Q for the 23.0 Pa case in Fig. 8 (ignoring some high Q noise in the 7.0 Pa data) that is primarily responsible for the 23.0 Pa sample giving the largest total surface area value in Table 1. Even though the other samples exhibit stronger Porod scattering for other Q orientations (Figs. 9 and 10), on averaging the Porod scattering over all solid angles, the Q orientation associated with Fig. 8 has by far the greatest weight in the orientationally-averaged surface area obtained. Meanwhile, the scattering curve for the intermediate pressure case (13.0 Pa) strongly suggests that the two columnar pore populations (large inter-columnar and fine intra-columnar) are not clearly delineated in size. Furthermore, the scattering intensity at the lowest Q values is 5–10 times less than for the other two conditions, suggesting a reduced fraction of the very largest columnar pores ($>100 \text{ nm}$ opening dimension and $>1 \mu\text{m}$ length).

When the Q direction was aligned at 30° to the substrate (case II, shown in Fig. 9) the scattering intensity curves at low Q show some of the same behavior seen in case I for the larger inter-columnar pores, but this is now constrained to $Q < 0.005 \text{ nm}^{-1}$, since the Q orientation is less favorable for columnar pore scattering. At higher Q values (0.005 – 0.05 nm^{-1}) the scattering for the 23.0 Pa high pressure case exhibits $Q^{-1.5}$ power law scattering while over a more restricted range (0.005 – 0.02 nm^{-1}) $Q^{-2.5}$ scattering is observed for the two lower pressures. These fractal scaling power laws can be associated with aspects of the column/feather coating morphologies seen in the SEM images, Fig. 5. The Q values in which the power law scattering is most prevalent are indicative of scattering from pores with mean opening dimensions in the 50 – 100 nm range. At this Q orientation, scattering from the feather pores gives rise to a clear interference peak (maximum) for the low and intermediate pressure cases. The data also suggests the presence of one for

the sample deposited at 23.0 Pa , although the scattering clearly suggests a broader size distribution in this sample. The presence of interference peaks indicates the existence of periodic spacing between the feather pores. It is important to note that for this Q orientation, Q is only perpendicular to a small fraction of the feather pores, because these are arranged at 60° to the substrate normal in all directions around it in the substrate plane, not just that defined by a particular Q direction. Nevertheless, since the orientation of the substrate is similar to the orientation of the feathery pores found on the coating columns, it is reasonable to attribute the interference peaks to the distinct feathers observed on the columns of these coatings. The position of these peaks in Q is related to the spacing of the periodicity, which is given by $2\pi/Q$. Thus, the feather pore periodicities with their estimated standard deviation uncertainties can be derived as: $(106 \pm 7) \text{ nm}$, $(112 \pm 7) \text{ nm}$, and $(70 \pm 10) \text{ nm}$, respectively for the 7.5 Pa , 13.0 Pa and 23.0 Pa conditions. More significantly, the intensity of the scattering around the peak for the intermediate pressure condition, 13.0 Pa , is about 2.5 times that for the other conditions. This suggests a greater level of fine feather porosity for the intermediate pressure condition, but the 23.0 Pa condition clearly has the most coarse feather porosity.

Interestingly, in case III (shown in Fig. 10), where the scattering is a measure of the structural variation through the coating thickness, e.g., from pores with their large dimensions parallel to the substrate surface, the 13.0 Pa sample also showed greatly increased scattering intensity for intermediate Q values ($0.01 \text{ nm}^{-1} < Q < 0.2 \text{ nm}^{-1}$) compared to the other pressure conditions, and significant interference peaks remained for all 3 samples. With Q perpendicular to the substrate, the preferred alignment planes of all of the feather features are about 60° off from the substrate plane. The interference scattering from the fine feather pore periodicity is actually more enhanced and more precisely defined than for case II. From the position of the interference peaks in Q , the apparent repeat distances (with their estimated standard deviation uncertainties) in the direction normal to the substrate are: $(151 \pm 5) \text{ nm}$, $(134 \pm 5) \text{ nm}$ and $(78 \pm 7) \text{ nm}$, respectively for 7.5 Pa , 13.0 Pa and 23.0 Pa . Multiplying by a factor of $\{\cos 60^\circ\}$, the derived repeat distances along a direction at 30° to the substrate are: $(76 \pm 3) \text{ nm}$, $(68 \pm 3) \text{ nm}$ and $(39 \pm 4) \text{ nm}$. These values give the average repeat distance for all of the fine feather periodicity for each pressure condition, rather than just those along the particular direction at 30° to the substrate given by case II. More importantly, the case III data confirm the prominence of the fine feather porosity in samples deposited at the intermediate pressure. This pore population presents significantly greater void surface area resolved perpendicular to any transport process in the substrate normal direction. The positions of the interference peaks still suggest that the finest feather pores occur for the 23.0 Pa condition. Also this Q orientation is not so favorable for scattering from the broad distribution of coarse feather pores in this sample.

Information concerning the shape and orientation distribution of the pores was also obtained by observing the change in the scattering intensity as a function of the specimen orientation for constant values of Q . Three Q ranges were investigated: (i) 0.006 – 0.008 nm^{-1} , (ii) 0.03 – 0.04 nm^{-1} and (iii) 0.09 – 0.10 nm^{-1} . Since X-ray scattering occurs when solid/gas interfaces are aligned perpendicular to the Q direction, measurements at different Q values provide information about the shape and orientation distribution of the pore opening dimensions at three different length scales. Within the context of the DVD void morphology apparent in Figs. 5 and 6, we attribute these to be: (i) mean opening dimensions: ≈ 100 – 250 nm , such as might be found for column dimensions 1 – $2 \mu\text{m}$, or more; (ii) mean opening dimensions: ≈ 35 – 70 nm , such as might apply for fine intra-columnar voids or feather pores of large dimensions 400 – 500 nm ; (iii) mean opening dimension ≈ 15 – 30 nm corresponding to fine feather features perhaps with

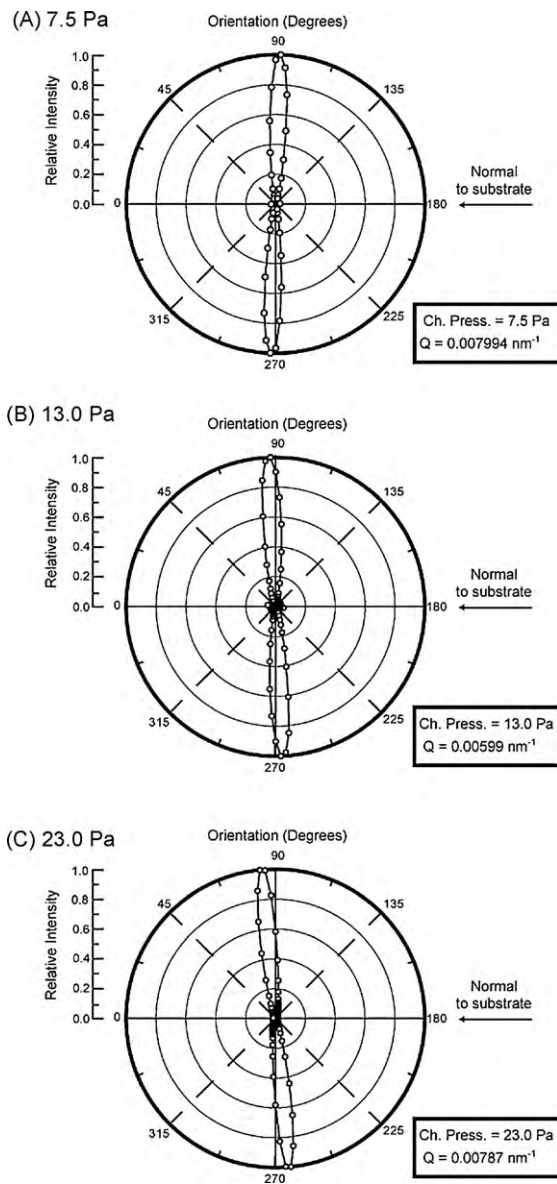


Fig. 11. Anisotropic scattering intensity distributions at constant Q with Q between $\approx 0.006 \text{ nm}^{-1}$ and $\approx 0.008 \text{ nm}^{-1}$ for coatings grown at: (a) 7.5 Pa, (b) 13.0 Pa and (c) 23.0 Pa. Statistical uncertainties are smaller than the symbols.

large dimensions 150–170 nm. Polar plots for the three Q values and each pressure condition are given in Figs. 11–13. As these plots show, alignment of the sample sections to give the substrate normal along $\alpha = 0^\circ$ was not perfect. However, this approximate 5° misalignment was taken into account in selecting the Q orientations for the data shown in Figs. 8–10, in order to capture the salient features from these anisotropic plots. For example, two of the datasets shown in Fig. 8 were offset in α from the nominal $\alpha = 90^\circ$ specified in order to capture fully the lobes exhibited in the anisotropic plots of Figs. 11–13.

The results indicate that for (i) (Fig. 11) the largest features have their opening dimensions in the plane of the substrate (in all azimuthal directions). This is consistent with the columnar pores being elongated approximately perpendicular to the substrate. Thus, scattering in this case is primarily due to the inter-columnar pores found in these coatings. In the anisotropic scattering measurements using an intermediate Q value (ii) (Fig. 12) increased intensity is observed for planar pores aligned 60° away from the substrate surface plane-normal (30° out of the substrate) and at

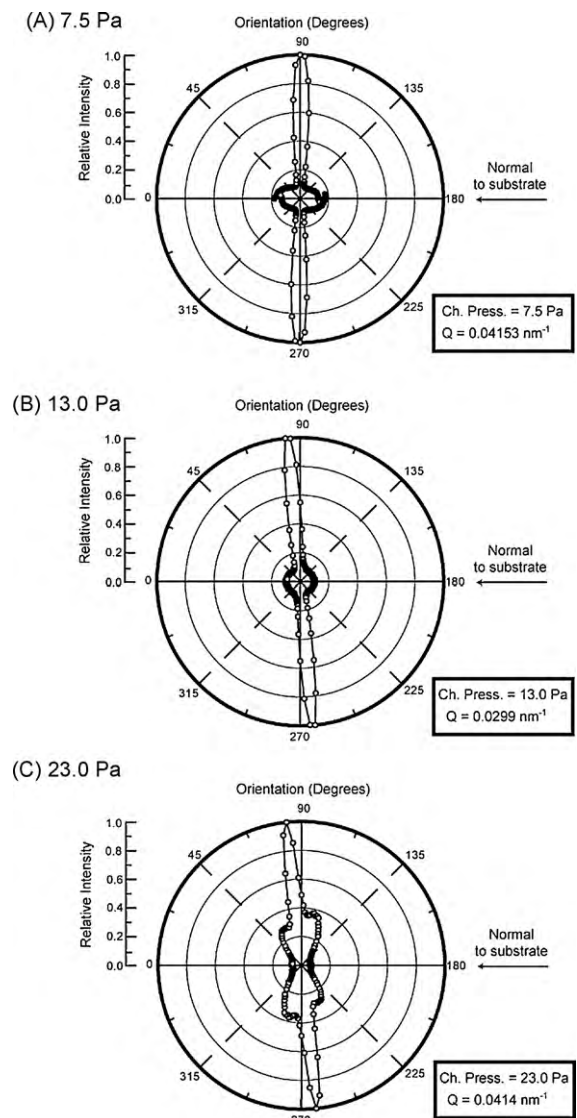


Fig. 12. Anisotropic scattering intensity distributions at constant Q , with Q between $\approx 0.03 \text{ nm}^{-1}$ and $\approx 0.04 \text{ nm}^{-1}$ for coatings grown at: (a) 7.5 Pa, (b) 13.0 Pa and (c) 23.0 Pa. Statistical uncertainties are smaller than the symbols.

60° from the substrate plane-normal at 0° , at least for the high pressure condition. Such scattering correlates with the coarser feathery features observed on the sides of the columns. This observation is supported by the strong scattering detected for the highest pressure condition (23 Pa) where the feathery features are pronounced (see Fig. 5c) and the virtual absence of the 60° scattering increase for the lowest pressure (7.5 Pa) condition where relatively smooth column surfaces are observed (see Fig. 5a). For the measurements using the largest Q values (iii) (Fig. 13) the greatest scattering still occurs from pores aligned perpendicular to the substrate, however, some scattering from fine scale feathery pores are also observed at the highest pressure condition. In addition, the low and intermediate pressures also show scattering from more randomly distributed or fine globular pores as scattering intensities are increased for the directions away from the column axis.

Previous studies of EB-PVD coatings have applied an anisotropic multi-component 3-dimensional microstructural model to fit the USAXS data simultaneously for several non-equivalent Q and sample orientations, subject to the constraints provided by requiring the anisotropic scattering to be reproduced at various Q values, such as given here in Figs. 11–13 [49]. Unfortunately, this was pre-

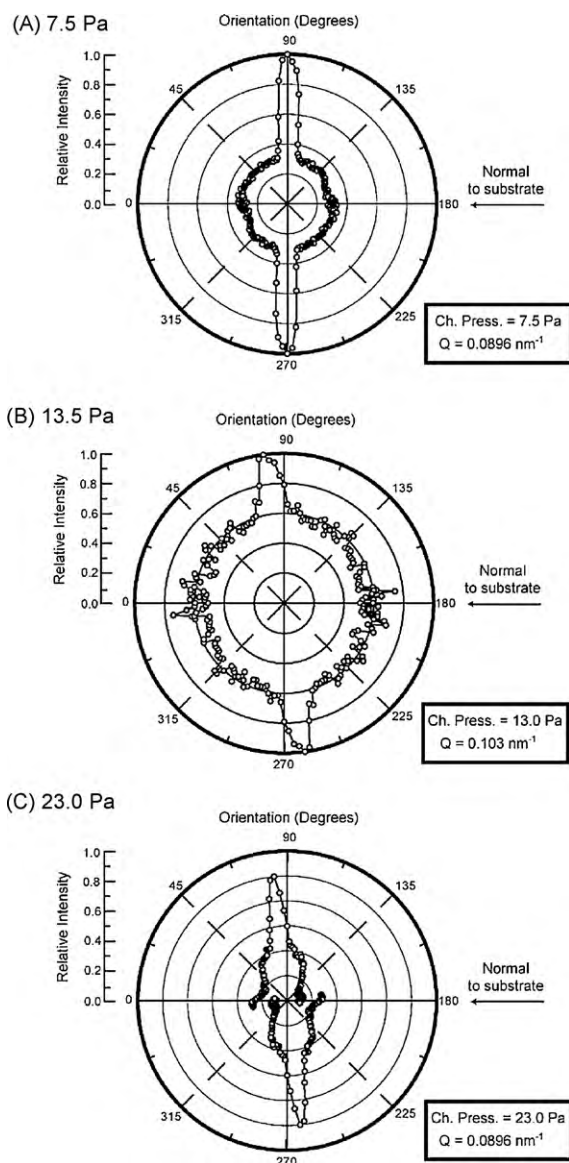


Fig. 13. Anisotropic scattering intensity distributions at constant Q , with Q between $\approx 0.09 \text{ nm}^{-1}$ and $\approx 0.10 \text{ nm}^{-1}$ for coatings grown at: (a) 7.5 Pa, (b) 13.0 Pa and (c) 23.0 Pa. Statistical uncertainties at this Q are more significant, and are indicated by the scatter in the points plotted.

cluded in the present studies due to the presence of the strong interference peaks in much of the USAXS data. The data for Q parallel to the substrate (Fig. 8) were not affected by interference peaks, and so these data were fitted using the entropy maximization routine, MaxEnt [50], to obtain apparent volume fraction size distributions. The fits are included in Fig. 8. Such size distributions are not realistic since they do not take into account the shapes of the pores, nor do they make any allowance for the strongly anisotropic pore orientation distributions. Nevertheless, for columnar pores aligned perpendicular to the substrate (opening dimensions in the substrate plane) these fits indicated (i) the largest fine columnar porosity and the smallest coarse columnar porosity occur for the intermediate pressure condition; (ii) the fine columnar pores have opening dimensions in the range 18–36 nm; and (iii) the coarse columnar pores have opening dimensions in the range 100–225 nm.

Finally, the measured densities of the coatings, given in Table 3, were found to correlate well with the anisotropically averaged Porod scattering pore surface area measurements as

Table 3

Thermal conductivity and density of YSZ samples.

Sample	Chamber pressure (Pa)	Thermal conductivity ($\text{W m}^{-1} \text{K}^{-1}$) ($\pm 0.1 \text{ W m}^{-1} \text{K}^{-1}$)	Density (g cm^{-3})
A	7.5	1.2	4.4
B	13	0.9	3.7
C	23	1.1	3.4

Uncertainties given are the estimated standard deviations, as discussed previously.

the coating density systematically decreased with chamber pressure.

3.3. Thermal conductivity measurements

The measured thermal conductivity of the coatings is given in Table 3. The results indicate that the lowest thermal conductivity ($0.9 \text{ W m}^{-1} \text{K}^{-1}$) was found for the sample grown using an intermediate pressure condition (13 Pa) which, from the USAXS data, contained a high proportion of fine pores inclined to impede heat flow. This result contrasts with the pore surface area and density measurements, which revealed a steady increase in the overall pore surface area and porosity (decrease in density) with chamber pressure.

4. Discussion

Large changes in the morphology of the multi-scale porosity were observed in DVD 7YSZ coatings deposited at different chamber pressures. As the deposition pressure was increased, these changes included an increased total pore surface area for pore diameters in the range of 10 nm to $2 \mu\text{m}$, a decrease in the coating density and an increase in the size of the feathery features found on the sides of the individual columns. USAXS data indicated that the largest size columnar pores analyzed (1–2 μm) were preferentially elongated perpendicular to the substrate for all pressures. This is consistent with microscopy, Fig. 5, which shows that many of the larger pores were oriented perpendicular to the substrate and located between both primary and secondary growth columns. The data also indicate increased scattering intensities from pore orientations aligned at 60° to the substrate surface for both the intermediate and high pressure cases. Such pores were observed to be coarser (they were observed at smaller Q) in the sample grown using the highest pressure. However, the USAXS data indicate that a finer scale of feathery porosity exists which was not resolvable by scanning electron microscopy. The USAXS measurements indicated that the volume fraction of the inter-columnar voids depended upon pressure. The highest volume fraction of these coarse inter-columnar voids was observed in the lowest chamber pressure case (in agreement with earlier observations [33]). At the finest pore scale (<60 nm) randomly distributed or globular pores were observed. The largest volume fraction of this pore fraction was observed in the sample grown at the intermediate pressure.

Pore formation in vapor deposited coatings depends strongly on the substrate surface geometry, the incident angle distribution (IAD) of the depositing atoms (or molecules) and the factors which affect the adatom surface mobility of the depositing material (i.e. the vapor species translation energy, the latent heat of condensation release, the degree of cluster formation in the vapor phase together with the substrate temperature, deposition rate and surface topology). In general, pores nucleate when regions on the substrate are depleted in incident vapor flux with respect to neighboring regions due to inhomogeneities on the substrate surface which results in the “flux shadowing” of local substrate regions. As the IAD distribution becomes broader and more asymmetric,

flux shadowing will increase and pores will nucleate more readily. These effects are limited, however, by the diffusion of adatoms across the growth surface into flux-depleted regions. Once nucleated the pore geometry during atomistic deposition is governed by the IAD distribution. In the case where clusters of atoms deposit upon a surface the size and geometry is more likely to be determined by the characteristics of the cluster impact.

The change in the coating microstructure observed as a function of DVD processing conditions may be related to several factors including the change in the gas jet conditions during coating deposition (i.e. the chamber pressure and pressure ratio) and likely a change in the size and volume of gas phase clusters of atoms [33]. The increased chamber pressure during DVD deposition alters the mean-free-path of vapor molecules and, along with the gas jet pressure ratio, the speed distribution of the background gas. This combination controls the distribution of incidence angles of the depositing atoms, molecules and clusters. For such an environment, Direct Simulation Monte Carlo models have indicated that the increased collision frequency observed when the chamber pressure is increased results in a broader IAD distribution [33]. Atomistic models have revealed that changes to these distributions will result in changes to the coating microstructure [24]. This change includes an increase in the total pore volume fraction and in the increased occurrence of feathery features on the sidewalls of the columnar features as the background pressure is increased. However, these models provide little insight into the phenomena that govern the formation of side arms on the primary columns and therefore periodic spacing of the feathery pores.

The nucleation and growth of clusters of atoms/molecules in the vapor phase can also be qualitatively related to the gas jet properties. For this case, the upstream pressure, gas jet speed, vapor density and chamber pressure can all play a role. Arguably, the upstream pressure (i.e. the pressure upstream of the choke point for the gas jet) is most critical as this is the pressure directly above the evaporation source where the vapor is the densest and the probability of cluster nucleation is highest. In this work, the upstream pressure was highest in the intermediate and low chamber pressure conditions. Following nucleation the vapor phase growth of nucleated clusters would depend upon the chamber pressure and gas jet speed. Increased pressures and low gas speeds lead to a reduced mean-free-path and a longer residence time to promote cluster growth. Of the highest cluster nucleation conditions (i.e. the low and intermediate chamber pressure cases) the intermediate chamber pressure case has the shortest mean-free-path and lowest gas jet speed and thus, it appears feasible that the population and size of vapor phase clusters which can impact the substrate during the deposition process is most likely to be highest for the 13 Pa intermediate pressure condition.

When clusters impact on a substrate their affect on the coating growth process is determined by their kinetic energy and the cohesion energies of the substrate. Several possibilities exist, including implantation of the cluster into the substrate, dissociation upon impact, or the formation of mounds on the surface. For the present case, low energy cluster impacts are most likely [29]. Mounds on the surface are then expected. When the cluster size is small, the mounds will affect the adatom surface mobility. For an adatom to diffuse over a mound the activation barrier for an atom jump over a ledge (i.e. the Schwoebel barrier) must be overcome. This barrier is much greater than for hopping over a flat surface and thus, surface diffusion will be reduced. As the frequency of cluster impacts and the cluster size increase, the process is no longer governed by the surface adatom diffusion, but increasingly by the successive cluster impacts. In such a case, very finely space globular pores may result.

Based on existing data it is not clear whether the finest scale porosity is the result of very fine feathery porosity or more globular fine scale pores, or a combination of both. In any event, it is impor-

tant to note that the shape and volume of this fine scale porosity appear to be responsible for the USAXS interference peak which is most strongly observed in the intermediate pressure case (13 Pa). This strong interference was correlated with a strong [1 1 1] growth column texture. The observation that the coating thermal conductivity does not decrease linearly with the pore surface area, but instead displays its lowest value at an intermediate pressure is consistent with the data shown in Fig. 10. These data indicate that when the samples were orientated with \mathbf{Q} perpendicular to the substrate, the highest scattering intensity from fine scale pores (20–70 nm in opening dimension) occurred from the coating deposited at the intermediate chamber pressure of 13.0 Pa. This is a result of the different shape and orientation distribution of the pores in the intermediate pressure case, as can be seen in Fig. 13, where the significant scattering from randomly oriented or globular shaped pores is observed for the intermediate pressure case.

Finally, some comment is warranted on how the scattering results for DVD coatings compared with similar data published previously on EB-PVD coatings [34,49]. While the results for these DVD coatings are generically similar, two important differences are observed. There is an enhanced ordering in the main columnar morphology, as evidenced by the narrowness of the anisotropic scattering shown in Figs. 11 and 12. There is also a greater regularity in the separation distance between the inclined planes of feather pores (or planes of feather pores), as evidenced by the prominence of the interference peaks shown in Figs. 9 and 10. As stated above, the prominence of the interference peaks precludes some of the more quantitative analysis carried out on the USAXS data from EB-PVD coatings [49]. However, these stronger and more ordered anisotropies for DVD (clearly apparent in the scattering), taken together with the greater microstructure – processing control described earlier, offer the prospect for better TBC performance and reliability using the DVD coating route.

5. Conclusions

A combination of USAXS, SEM, density and thermal conductivity measurements of porous 7YSZ coatings deposited using a directed vapor deposition technique reveal that the volume fraction and orientation of the pores, and thus the coatings' thermal conductivity, can be manipulated by the pressure within the deposition system. It is found that:

1. The pore surface area increases monotonically with increase in the deposition pressure and is correlated with a monotonic reduction in overall coating density.
2. The X-ray scattering intensity from ellipsoidal pores aligned with their large dimensions parallel to the substrate surface was greatest for coatings deposited using an intermediate pressure of 13 Pa. The X-ray scattering intensity for samples grown at an intermediate pressure (13.0 Pa) was about 2.5 times that for the other conditions suggesting a much greater fraction of feathery porosity for the intermediate pressure condition.
3. The lowest thermal conductivity was measured in the sample deposited at the intermediate pressure of 13 Pa. The USAXS measurements indicated that the voids in this sample presented the highest void surface area resolved in the plane of the coating and thus the most effective barrier to through-thickness heat transport.

The results indicate that the USAXS technique provides an effective tool for obtaining volumetric averages of the pore features responsible for the thermal conductivity of porous coatings.

Acknowledgements

We are grateful to the Office of Naval Research for support of this research under ONR Grant N00014-03-1-0297 monitored by Dr. David Shifler. Use of the Advanced Photon Source was supported by the U.S. Department of Energy, Office of Science, Office of Basic Energy Sciences, under Contract No. DE-AC02-06CH11357. We thank Dr. J. Ilavsky, Advanced Photon Source, Argonne National Laboratory, for help with the USAXS measurements.

References

- [1] J.W. Fairbanks, R.J. Hecht, *Mater. Sci. Eng.* 88 (1987) 321.
- [2] NRC, *Coatings for High-Temperature Structural Materials: Trends and Opportunities*. Washington, DC, National Academy of Sciences (1996). ISBN 0-309-05381-1.
- [3] R.L. Jones, Thermal barrier coatings, in: K.H. Stern (Ed.), *Metallurgical and Ceramic Protective Coatings*, Chapman and Hall, London, 1996, p. p. 194.
- [4] N.P. Padture, M. Gell, E.H. Jordan, *Science* 296 (2002) 280.
- [5] D.R. Clarke, C.G. Levi, *Ann. Rev. Mater. Res.* 33 (2003) 383.
- [6] D.R. Clarke, S.R. Phillpot, *Mater. Today* (June) (2005) 22–29.
- [7] D.R. Clarke, *Surf. Coat. Technol.* 163–164 (2003) 67–74.
- [8] C.G. Levi, *Curr. Opin. Solid Mater. Sci.* 8 (2004) 77–91.
- [9] J.R. Nichols, et al., *Surf. Coat. Technol.* 151–152 (2002) 383.
- [10] H.-S. Yang, G.-R. Bai, L.J. Thompson, J.A. Eastman, *Acta Mater.* 50 (2002) 2309.
- [11] P.G. Klemens, *High Temp. High Press.* 17 (1985) 41.
- [12] S. Gu, T.J. Lu, D.D. Hass, H.N.G. Wadley, *Acta mater.* 49 (2001) 2539–2547.
- [13] T.J. Lu, C.G. Levi, H.N.G. Wadley, A.G. Evans, *J. Am. Ceram. Soc.* 84 (2001) 2937–2946.
- [14] J.T. Demasi, M. Ortiz, K.D. Sheffler, NASA CR 182230 (1989).
- [15] R.A. Miller, G.W. Leissler J.M. Jobe, NASA TP 3285 (1993).
- [16] A. Kyoungjun, K.S. Ravichandran, S.L. Semiatin, *J. Am. Ceram. Soc.* 82 (1999) 299.
- [17] S.M. Meier, D.K. Gupta, *Trans. ASME* 116 (1994) 250.
- [18] X.W. Zhou, R.A. Johnson, H.N.G. Wadley, *Acta Mater.* 45 (11) (1997) 4441.
- [19] K.H. Müller, *Surf. Sci.* 184 (1987) L375.
- [20] S.M. Rossmagel, C. Nichols, S. Hamaguchi, D. Ruzic, R. Turkot, *J. Vac. Sci. Technol. B* 14 (1996) 1819.
- [21] J.G.W. van de Waterbeemd, G.W. van Oosterhout, *Phillips Res. Reps.* 22 (1967) 375.
- [22] J.A. Thornton, *J. Vac. Sci. Technol.* 12 (1975) 830.
- [23] K. Kennedy, *Proceedings of the AVS Vacuum Metallurgical Conference*, Los Angeles, 1968, 195.
- [24] K.H. Müller, *J. Appl. Phys.* 58 (1985) 2573.
- [25] J.J. Cuomo, J.M.E. Harper, C.R. Guarnieri, D.S. Yee, L.J. Attanasio, J. Angilello, C.T. Wu, R.H. Hammond, *J. Vac. Sci. Technol.* 20 (1982) 349.
- [26] T.C. Huang, G. Lim, F. Parmigiani, E. Kay, *J. Vac. Sci. Technol. A* 3 (1985) 2161.
- [27] B.V. Movchan, A.V. Demchishin, *Phys. Met. Metallogr.* 28 (1969) 83.
- [28] D.V. Rigney, R. Viguie, D.J. Wortman, D.W. Skelly, *Thermal Barrier Coating Workshop 1995*, NASA Conference Publication 3312 (1995) 135.
- [29] K. Robbie, L.J. Friedrich, S.K. Drew, T. Smy, M.J. Brett, *J. Vac. Sci. Technol. A* 13 (1995) 1032.
- [30] Y.G. Yang, R.A. Johnson, H.N.G. Wadley, *Acta Mater.* 45 (1997) 1455.
- [31] H. Zhao, F. Yu, T.D. Bennett, H.N.G. Wadley, *Acta Mater.* 54 (2006) 5195–5207.
- [32] D.D. Hass, H.N.G. Wadley, *J. Vac. Sci. Technol. A* 27 (2009) 404–414; G.A. Bird, *Molecular Gas Dynamics and the Direct Simulation of Gas Flows*, Clarendon Press, New York, 1994.
- [33] D.D. Hass, Y.Y. Yang, H.N.G. Wadley, *J. Porous Mater.* 17 (2010) 27.
- [34] A. Kulkarni, A. Goland, H. Herman, A.J. Allen, T. Dobbins, F. DeCarlo, J. Ilavsky, G.G. Long, S. Fang, P. Lawton, *Mater. Sci. Eng. A* 426 (2006) 43.
- [35] J.F. Groves, G. Mattausch, H. Morgner, D.D. Hass, H.N.G. Wadley, *Surf. Engin.* 16 (2000) 461.
- [36] J.F. Groves, Y. Marciano, D.D. Hass, G. Mattausch, H. Morgner, H.N.G. Wadley, *Proceedings of the Society of Vacuum Coaters 44th Annual Technical Conference* (2001) 99.
- [37] J. Ilavsky, A.J. Allen, G.G. Long, P.R. Jemian, *Rev. Sci. Instrum.* 73 (2002) 1660.
- [38] J. Ilavsky, P.R. Jemian, A.J. Allen, F. Zhang, L.E. Levine, G.G. Long, *J. Appl. Cryst.* 42 (2009) 469–479.
- [39] U. Bonse, M. Hart, *Appl. Phys. Lett.* 7 (1965) 238.
- [40] J. Ilavsky, P.R. Jemian, *J. Appl. Cryst.* 42 (2009) 347–353.
- [41] J. Ilavsky, G.G. Long, A.J. Allen, C.C. Berndt, *Mater. Sci. Eng. A* 272 (1999) 215.
- [42] W.J. Parker, et al., *J. Appl. Phys.* 32 (1961) 1679.
- [43] R.D. Cowan, *J. Appl. Phys.* 34 (1962) 926.
- [44] D.G. Cahill, *Rev. Sci. Instrum.* 61 (1990) 802.
- [45] ASTM Standard Test Method E 1225–87, *Annual Book of ASTM Standards*, ASTM, Philadelphia 14.02 (1994), p. 712.
- [46] ASTM Standard Test Method C 177–85, *Annual Book of ASTM Standards*, ASTM, Philadelphia 4.06 (1992), p. 17.
- [47] A.J. Slifka, B. J. Filla J. M. Phelps, in *Proceedings of the 1997 TBC Workshop*, Cincinnati, OH (1997), p. 33.
- [48] D.D. Hass, A.J. Slifka, H.N.G. Wadley, *Acta mater.* 49 (2001) 973–983.
- [49] A. Flores Renteria, B. Saruhan, J. Ilavsky, A.J. Allen, *Surf. Coat. Technol.* 201 (2007) 4781–4788.
- [50] J.A. Potton, G.J. Daniell, B.D. Rainford, *J. Appl. Cryst.* 21 (1988) (1988) 663–668.